Deposition effects and interface structure of HVOF-sprayed multimodal WC-CoCr coatings

Leyi Chang[1,2]**, Wenyan Wang**[1,2,a)] **, Douqin Ma**[1,2,a)]**, Jingpei Xie**[1,2]

[1] *School of Materials Science and Engineering, Henan University of Science and Technology, Luoyang 471023, Henan, China*
[2] *Provincial and Ministerial Co-Construction of Collaborative Innovation Center for Non-Ferrous Metal New Materials and Advanced Processing Technology, Henan University of Science and Technology, Luoyang 471023, Henan, China*
a) Address all correspondence to these authors. e-mails: wangwy1963@163.com; madouqin1987@163.com

The deposition behavior of WC-CoCr powder, microstructure, hardness and fracture toughness of the coating were examined. The splats and coatings were deposited on the surface of the Q235 steel by high-velocity oxygen-fuel spraying (HVOF). The multimodal WC-CoCr powders contained three sizes of WC particles of 1.5, 0.8 and 0.3 μm, with mass fractions of 15, 66 and 5%, respectively. The splats spread on the surface of substrate in wafer type and bubble-like type. The diffusion of the Fe, Cr and Co elements and depression deformation occurred near the interface between the splats and substrate. Fine grains were observed in the substrate near the interface. The main phases in the coating are WC, W_2C and Co_3W_3C. In addition, the microhardness of the coating is above 1000 HV0.3. The variation in microhardness is only 215.7 HV0.3. The fracture toughness of the coating is 4.45 MPa·m$^{1/2}$.

Introduction

WC-based coatings with high hardness, excellent wear and corrosion resistance were deposited on the surface of metal parts to enhance the life of parts (such as petroleum pipeline and undercarriage) [1–6]. WC-based coatings were often prepared by high-velocity oxygen-fuel spraying (HVOF), plasma spraying (PS), detonation gun spraying (DGS), and laser cladding (CL) [7–10]. HVOF with the advantages of low flame temperature, fast flame flow speed and fast particle flight speed is widely used in the preparation of WC-based coatings [11–15].

WC-based coatings are widely used in variety of industries, such as aerospace, petrochemical engineering and paper industry [16, 17]. Thermal spray WC-based coatings provide excellent wear resistance and corrosion resistance for industrial applications [18]. In recent years, research on WC-based coatings mainly focused on the influence of WC particle size on the microstructure and properties of the coatings. As the WC particle size decreases, the mean free path of the binder was decreased, resulting in an increase hardness of the coating [19, 20]. Moreover, the wear resistance of WC-based coatings increased with the decrease of WC particle size due to evenly distributed WC particle within the microstructure [21, 22]. However, other investigation showed that WC particle size decreases to nano-sized, the oxidation and decarburization of

WC particles are more pronounced during deposition, which decrease the wear resistance of WC-based coatings [23–25]. The decarbonization and dissolution of nano-sized WC into the binder increases the brittleness of the bond phase, resulting in a decrease in the wear resistance of the WC-based coating [18]. To meet the mechanical properties and wear resistance requirements for WC-based coatings, the study of bimodal and multimodal WC-based coatings has become a hot spot in the industry of preparing WC-based coatings in recent years [26, 27].

The spreading morphology of single spalt on the substrate or pre-deposited layer determines the coatings formation, and affects the microstructure and properties of the coating [28, 29]. The powders are heated and accelerated to a semi-molten sate and then rapidly deform and solidify to form a coating after being deposited on the surface of the substrate within a high speed [30–32]. After the spray gun is scanned on the surface of the substrate, a large number of splats accumulated and coating formed [33, 34]. The bonding between the splat and substrate is an important factor that determines the interface properties of coating and substrate. Therefore, it is very important to study the influence of single splat on the interface properties of substrate.

In this work, multimodal WC-CoCr powders were prepared by spray drying method. The powder prepared by spray drying method has the characteristics of high sphericity and high

fluidity, which is conducive to the spraying in the process of supersonic flame spraying. The multimodal WC-CoCr composite coating was manufactured by HVOF. The spreading morphology and interface bonding of splats on the substrate were observed by deposition a small amount of multimodal WC-CoCr powders. The transmission morphologies of splats and substrate near the interface were analyzed. The phase structure of powders and coating were characterized. The micromorphology and mechanical properties of multimodal WC-CoCr coating were observed. The strengthening and toughening mechanism of multimodal WC-CoCr coating was analyzed.

Results and discussion

Powder characteristics

Figure 1 shows that surface and cross-section microstructure of the multimodal WC-CoCr powders. The multimodal WC-CoCr powders has a spherical, loose and porous structure, as shown in Fig. 1(a). The porous structure of the multimodal WC-CoCr powders is conducive to improving the melting degree of powders and the deformation degree of splat [35]. The main phase of the multimodal WC-CoCr powders consists of WC, Co and Co_3W_3C [36]. Figure 1(b) shows the high magnification microstructure of the multimodal WC-CoCr powders. The gray area in SEM image is the Co-Cr binder phase, the brighter spots are WC particles. The micron-sized WC particles in the powders show irregular geometric shapes are observed. Figure 1(c) reveals the Point scanning of WC position (Point 1) and bonding phase position (Point 2) on the powders surface. It is found that

W, C, Co and Cr can be observed at both positions, indicating that the WC particles dissolves. W and C elements dissolve in the melting CoCr binder, leading to the formation of Co_3W_3C. The Cr has a strong affinity with C element and combines with a small amount of C element to form a chemical compound. However, the presence of Cr and Cr chemical compounds are not detected in the XRD pattern because the content is small [36]. Figure 1(d) indicates that the cross-section morphology of the powders, pores can be observed. The EDS of multimodal WC-CoCr powders cross-section is revealed in Fig. 1(e). The distribution of various elements is relatively uniform, with only a small amount of Co element has aggregation phenomenon.

Deposition behavior of splats

The formation process of the coating as found in Fig. 2. Figure 2(a) exhibits that the schematic diagram of multimodal WC-CoCr powders injects into the spray gun and accelerate by flame heating and then impinge on the substrate surface. The flame temperature in the process of spraying is about 2600 °C. The WC (melting point 2870 °C) particles are partially dissolved, while Co (melting point 1495 °C) and Cr (melting point 1857 °C) are completely dissolved into liquid phase. After being heated by flame flow, the multimodal WC-CoCr powders form semi-molten droplets. Then the WC-CoCr powers impinge on the substrate surface at high speed, the molten bonder phase solidifies rapidly after violent deformation. The connection of multiple splats forms a single coating, and then continue spray to form a coating with a thickness of about 200 μm, as shown in Fig. 2(b). The SEM image of single pass deposited on the
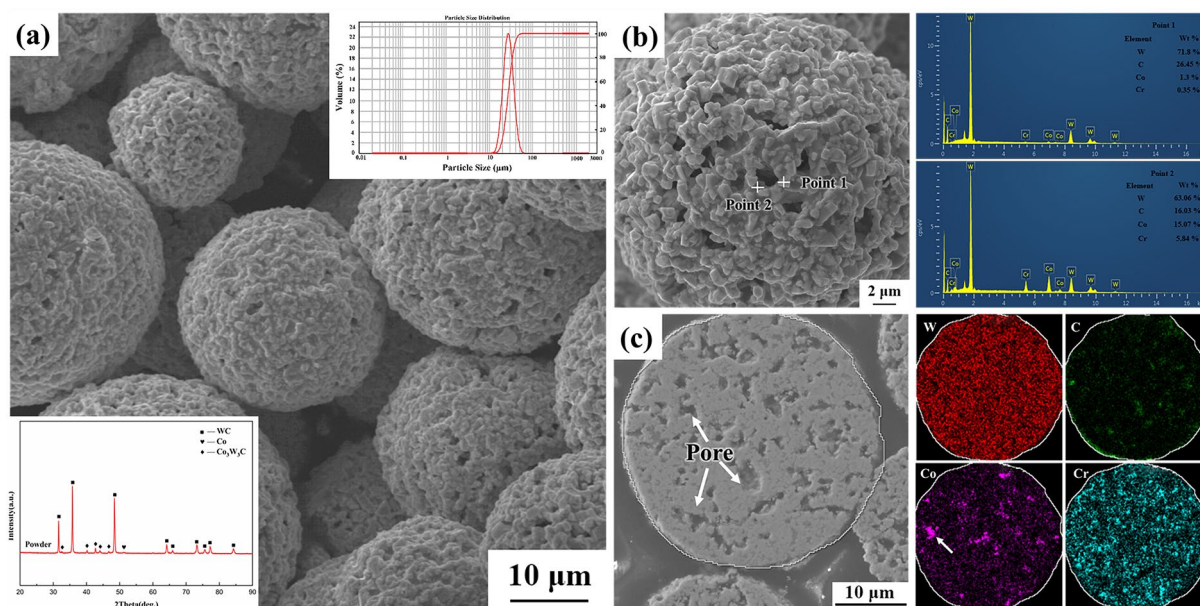

Figure 1: SEM image and XRD of multimodal WC-CoCr powders (a), high magnification morphology of multimodal WC-CoCr powders (b), EDS of Point 1 and Point 2 (c), SEM of multimodal WC-CoCr powders cross-section (d), and EDS of multimodal WC-CoCr powders cross-section(e).
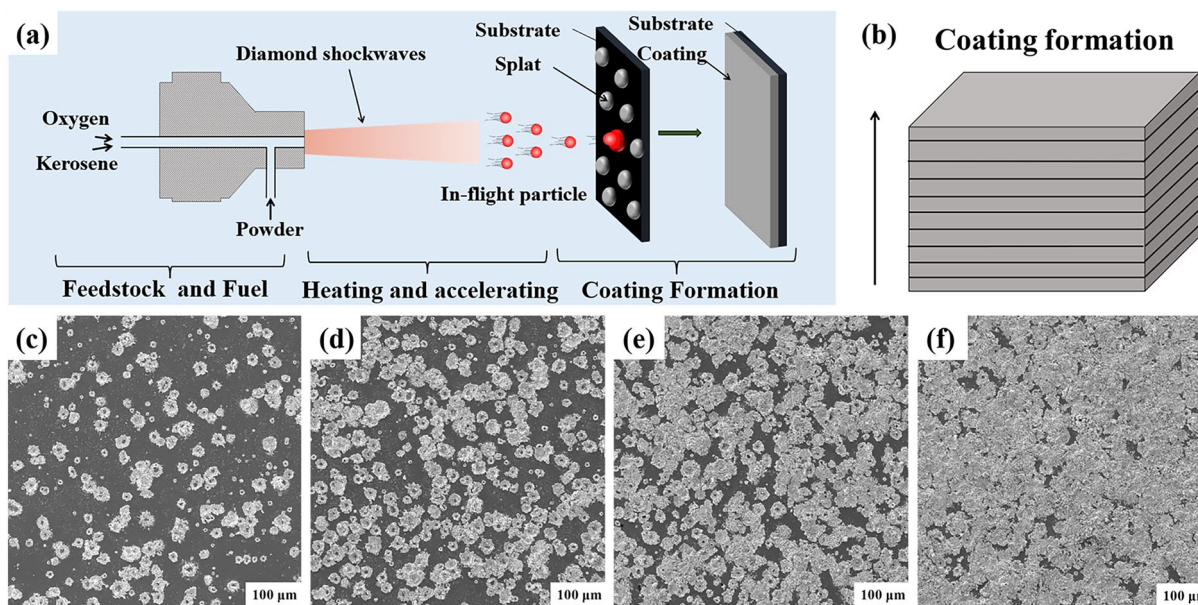
Figure 2: Diagram of powders deposition (a), diagram of coating formation (b), SEM of single pass deposited (c), SEM of two layers deposition (d), SEM of three layers deposition (e), SEM of four layers deposition (f).

surface of the substrate is shown in Fig. 2(c). The SEM images of two layers deposition, three layers and four layers are revealed in Fig. 2(d)–(f), respectively. With the increase of spraying passes, the number of splats deposited on the substrate surface increases.

Figure 3 shows the surface and cross-section morphology of splats spread on the substrate. It can be observed that splats mainly spread on the surface of substrate in the form of wafer type [Fig. 3(a)] and bubble-like type [Fig. 3(b) and (c)]. The multimodal WC-CoCr powders hit the substrate surface and underwent drastic plastic deformation. Disappearance of the spherical structure of multimodal WC-CoCr powders. The splats have no obvious central uplift phenomenon, which is differs from the results reported by Chen [37]. It's related to the higher melting degree of the multimodal WC-CoCr powders in this paper. The wafer type splat is regular in shape with small splash on the edge. A warping phenomenon occurs at the edge of the bubble-like splats. The material around the "Bubble" is sunken and well combine with the substrate, as shown in Fig. 3(b). However, the substrate binds poorly to the splats due to the material around "Bubbles" warps upward, as shown in Fig. 3(c). Microcracks are observed around the "Bubble". Figure 3(d)–(f) shows the cross-section SEM images of three kinds of splats, it can be observed that depression deformation occurs near the interface between splats and substrate. The spreading edge of the splats has varying degrees of warping and is incompletely bonded to the substrate. Furthermore, it is found that there are some deciduous WC-CoCr fragments, as shown in Fig. 3(f). It is associated with the spreading morphology of a single splat on the substrate. The

material around the "Bubble" presents warping phenomenon, resulting in a relatively loose bond with the substrate. During metallographic sample preparation, the material around the "Bubble" is easily peeled off from the substrate after friction. Due to the warping phenomenon caused by incomplete combination of splat and substrate, it will cause a "shadow effect" resulting in incomplete filling of the subsequent splat.

The mapping and cross section line scans of splats stacking are shown in Fig. 4. The surface SEM image of two spalts stacking is revealed in Fig. 4(a). It can be seen that two splats form a good combination. The elemental mapping reveal that a small amount of Fe is distributed uniformly in the center of the bubble-like type splat. In addition, a small amount of Fe element is enriched at the connection of the two splats. It is owing to the incomplete filling phenomenon in the connection position of the two splats. It should be attributed to the edge warping of splat. The subsequent splat filling at connection of the two splats is not complete, leading to Fe element enrichment at this position. The elements at other positions are evenly distributed without obvious segregation.

Figure 4(c) shows the cross-section SEM image of splats stacking and the line-scanning EDS analysis of the interface. The interface location is free of porosity as well as cracking defects. However, there are pores inside splats, it is associated with the original porous structure of the multimodal WC-CoCr powders and the semi-melting state in the spraying process. During the spreading process of the splats, the molten binder phase fails to fill the pores in the multimodal WC-CoCr powders to form pores in the splats. The
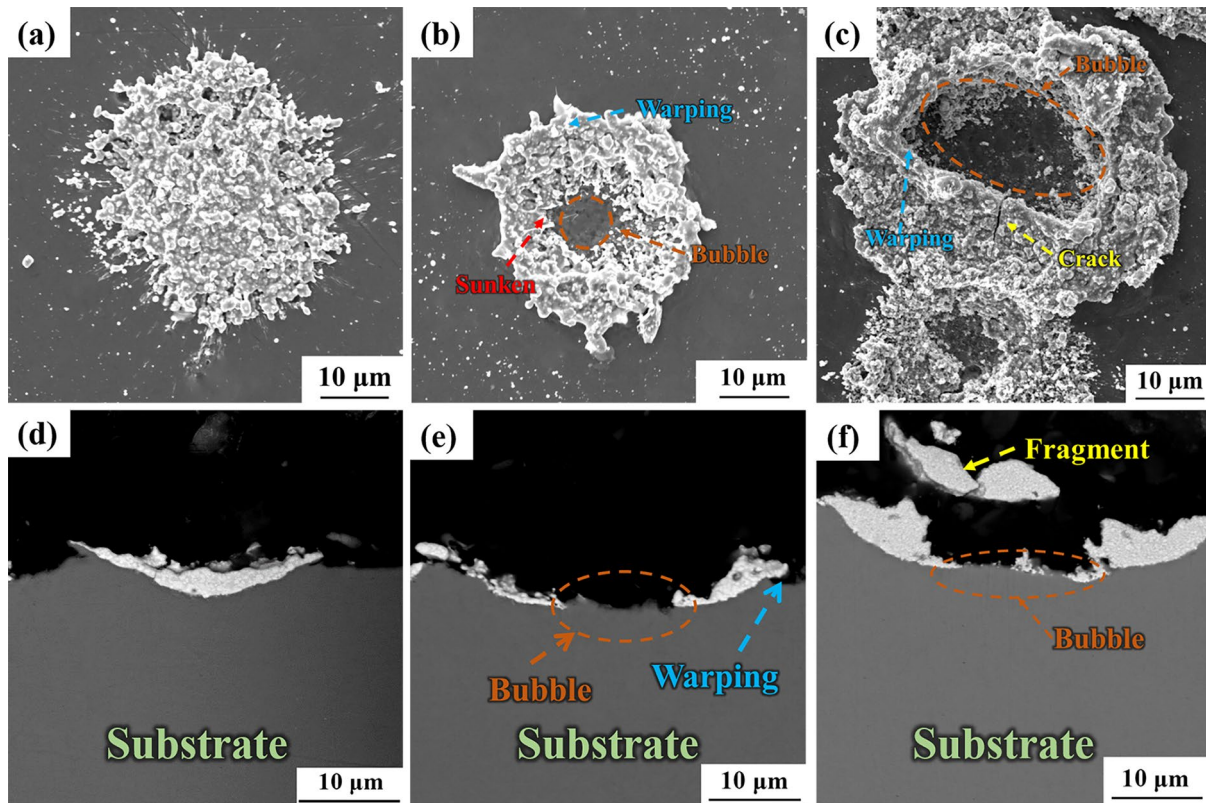
Figure 3: Surface and cross-section morphology of splats, wafer type (a, d), bubble-like type, (b, c, d, e).
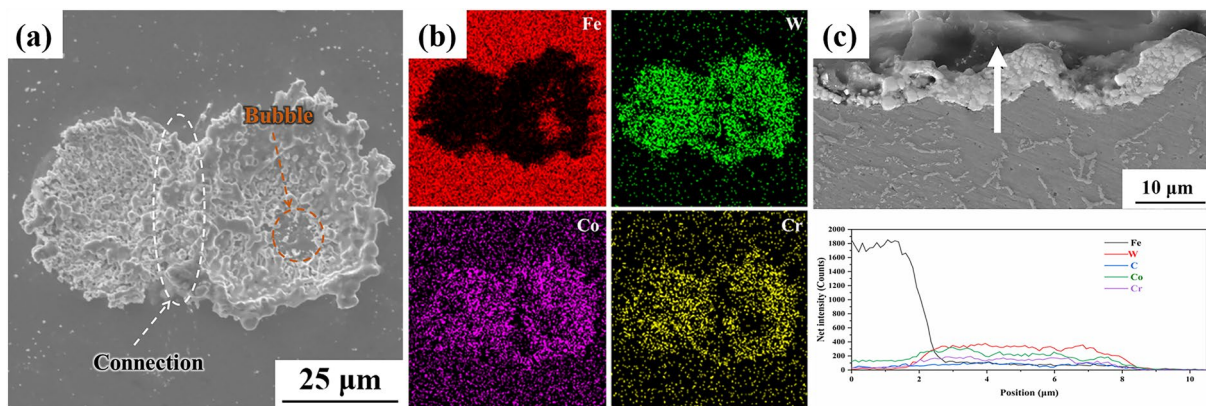

Figure 4: Mapping (a, b) and cross-section line scans (c) of splats stacking.

line-scanning of cross-section can be observed that there is a transition layer with a thickness of about 1 μm at the interface. It indicates that an elementary diffusion phenomenon has occurred between the splat and the substrate. There is a degree of metallurgical bonding at the interface between the splats and the substrate.

TEM analysis of interface between splats and substrate

Figure 5(a) shows a bright field TEM image of the bonding position of splat and substrate, which contains four different regions (i.e. regions A, B, C and D). The particle size distribution of WC is between 0.1 and 1.3 μm, which is slightly lower than that of WC in the multimodal WC-CoCr powders. It can also be seen
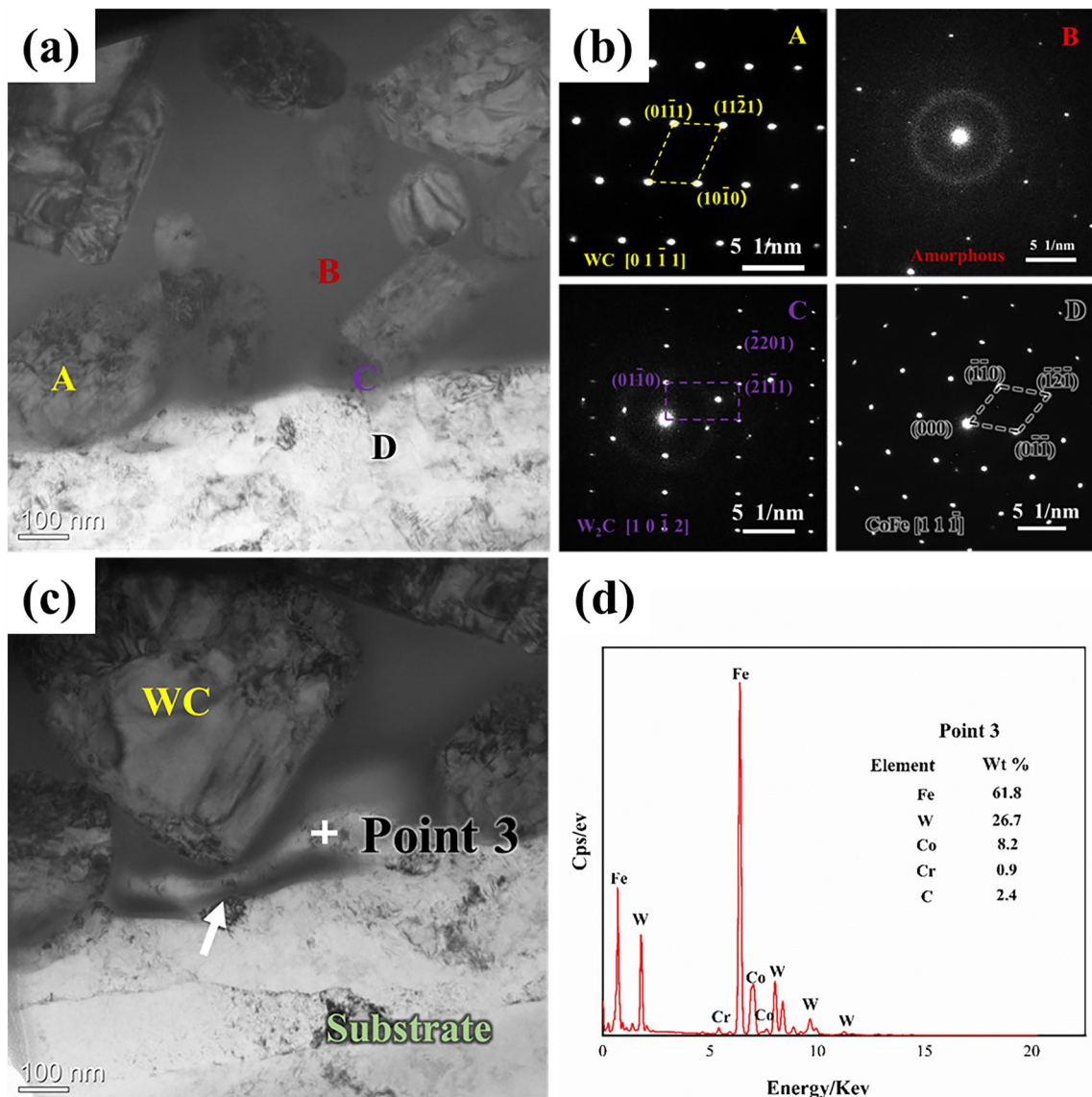
Figure 5: TEM of the bonding position of splat and substrate (a, c), SAED of A, B, C and D (b), and point scan of Point 3 (d).

that there are morphological changes in the WC particles when a comparison is made with the powders and the splats. Nano-sized WC particles mainly show an arc structure, while micron-sized WC particles still have a geometric structure. Nano-sized WC particles are evenly distributed around micron -sized and sub-micron -sized WC particles. It is attributed to a small amount of dissolution at the edges of the WC particles as they are heated by the flame. There is a continuous contact between the substrate and splat. The interface is defect free. Figure 5(b) shows the SAED diagram of A, B, C and D in Fig. 5(a). The information of crystal plane spacing and crystal plane parameters can be obtained by calibrating its crystallographic parameters. A is WC particle (hcp, a = b = 2.92832042, c = 2.85290700, α = β = 90°, γ = 120°), B is the amorphous phase formed after rapid cooling

of the CoCr bonding phase, C is the W_2C (hcp, a = b = 2.99704, c = 4.7279, α = β = 90°, γ = 120°) [2, 36]. In the single splat, W_2C is only observed at the edge of WC particles without individual W_2C in the bonder phase. W_2C is produced at the edge of WC particles without changing the original shape of WC particles. It has to do with the oxidation and decarbonization of WC particles by heat and oxygen. The phase of substrate region D is CoFe (bcc, a = b = c = 2.855, α = β = γ = 90°). According to the difference of atomic contrast, the diffusion phenomenon at the interface can be obviously observed, as shown by the arrow in Fig. 5(c). Figure 5(d) shows the EDS at point 3. W and Cr element can be observed, which further indicates that elements diffuse at the interface. The diffusion distance is limited, about 1um [as shown in Fig. 4(c)].
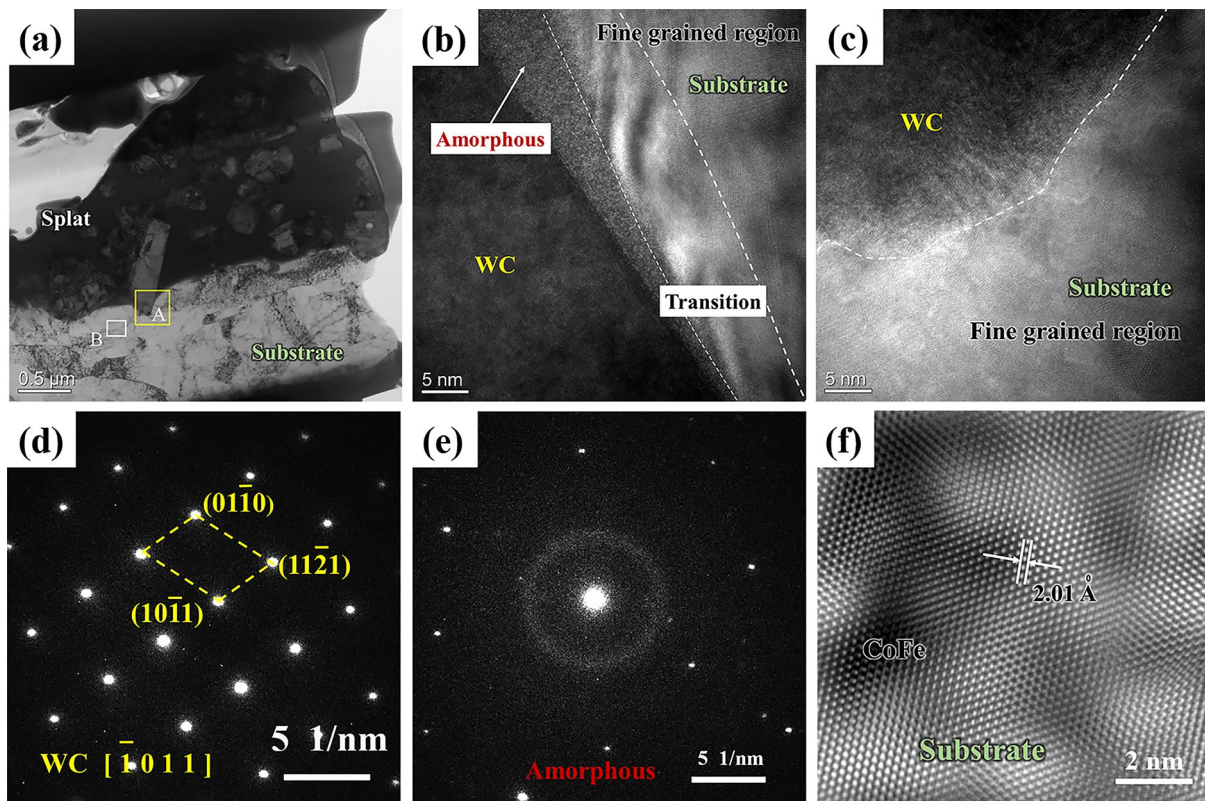
Figure 6: TEM of the bonding position of splat and substrate (a), HRTEM of A (b, c), SAED of WC (d) and amorphous (e), HRTEM of B (f).

The TEM images of the interface position of a splat with bubble-like type is shown in Fig. 6. It can be seen that WC particles with sharp angle shape can be directly embedded into the substrate at the interface position, as shown in region A. It is concerned with the high kinetic energy and temperature of semi-molten particles after heating and accelerating.

The HRTEM image at the boundary of WC particles is shown in Fig. 6(b). The interface between WC particle and the bonder phase is clear without obvious transition layer [2]. However, there is a transition layer of about 10 nm between the bonder phase and the substrate. Meanwhile, the substrate on the right of the transition layer forms an obvious fine-grained region. Figure 6(c) shows the HRTEM image of WC particle tip in region A. The WC particles are directly in contact with the substrate and the boundary at the interface is clear without obvious transition layer. The substrate near the interface presents fine-grained region. A high pulse pressure is generated at the impact position, high temperature and high pressure are generated locally in the substrate [38]. A lot of energy is transferred to the substrate surface, which causes deformation and produces grain refinement phenomenon of substrate [37]. The SAED of WC particles and amorphous phases are revealed in Fig. 6(d) and e respectively. Figure 6(f) shows the HRTEM image of the substrate at the region B. It can be observed that there is no fine-grained region in the substrate position away from the interface.

It indicates that the energy transferred to the substrate by splats is limited. The element diffusion and grain refinement only occur at a limited position near the interface.

Microstructure characteristics of the multimodal WC-CoCr coating

Surface and cross-sectional morphology of coating are shown in Fig. 7. The XRD pattern of the multimodal WC-CoCr coating is shown in Fig. 7(a). The main phases in the coating are WC, W_2C and Co_3W_3C. During the flight, the WC particles on the surface of the multimodal WC-CoCr powders come into contact with oxygen and undergo oxidative decarburization to produce W_2C ($2WC + O_2 \rightarrow W_2C + CO_2$). W_2C is distributed around the WC particles, as shown in Fig. 5(a). The high cooling rate of the molten CoCr bonder phase leads to the formation of an amorphous phase. It is shown in diffuse scattering peak at $2\theta \approx 45°$.

The local three-dimensional morphology of the coating surface is revealed in Fig. 7(b). The coating consists of multiple splats, it can be seen that the coating surface has a certain roughness. Pores and splats with poor melting can be observed on the coating surface, as is shown in Fig. 7(c). The WC particles are evenly distributed in bonder phase, but the WC particles in the poorly melted splats are in a raised state.
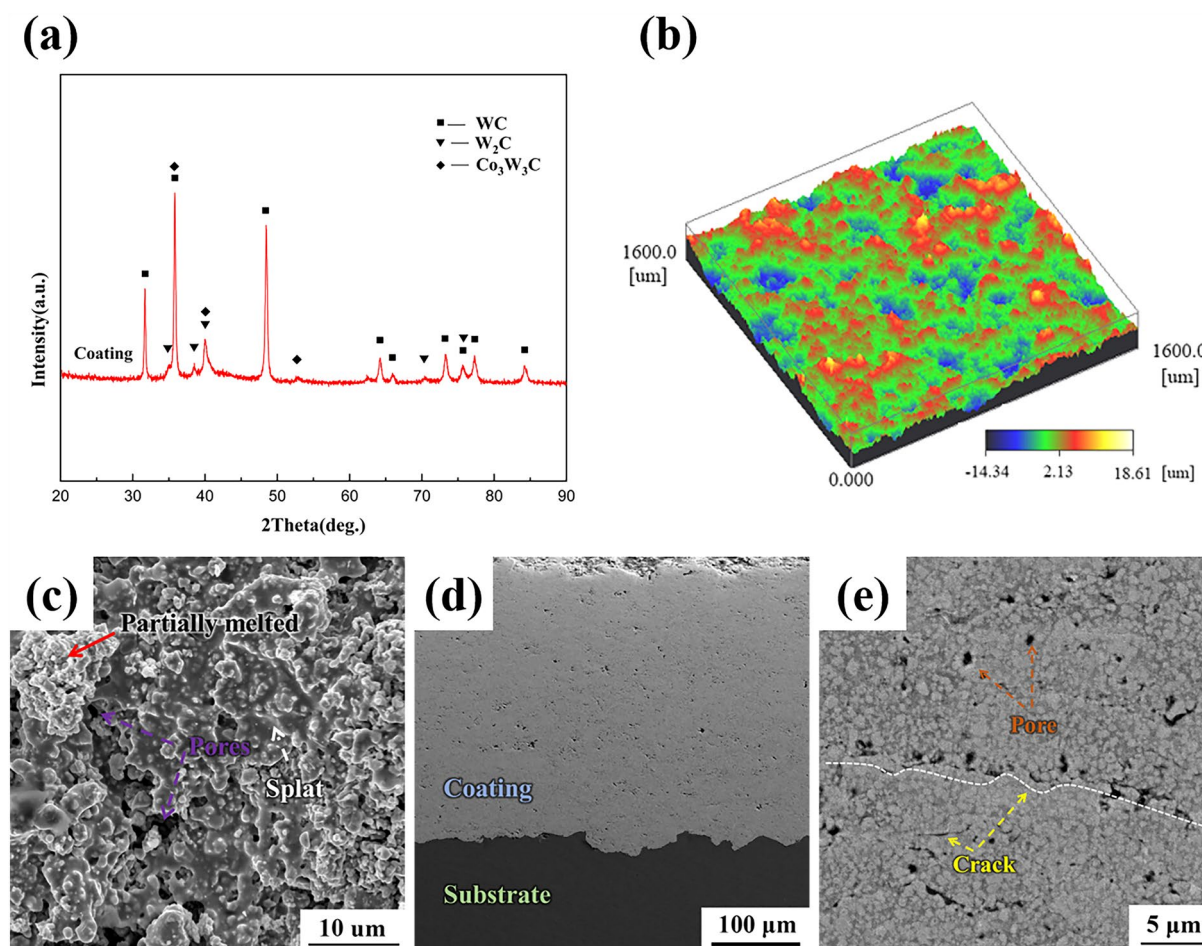
Figure 7: XRD of the multimodal WC-CoCr coating (a), three-dimensional morphology of the coating surface (b), microstructure of the coating surface (c), cross-section microstructure of the WC-CoCr coating (d, e).

Figure 7(d) and e show the SEM images of cross-section the multimodal WC-CoCr coating under different magnifications. There is a good bond between the coating and substrate without obvious defects such as pores, cracks and inclusions. Microcracks and pores can be observed in the coating section, as shown in Fig. 7(e). Meanwhile, microcracks are observed at the edges of the pores, it is because the presence of pores can lead to stress concentration and thus the formation of microcracks [39]. The porosity of the coating is shown in Table 1. The average porosity of the coating is 0.14%. This indicates that the coating is dense. The porosity of microstructure and nanostructure WC-CoCr coatings prepared by the same spraying parameters are 0.24 and 0.51%, respectively [40]. Compared with the WC-based coatings prepared by cold spraying and warm spraying, the density of the coatings prepared by HVOF is significantly higher [8, 41].

The mechanical properties of the coating are shown in Table 1. The average microhardness of the coating measured by Vickers microhardness tester is 1131.2 HV0.3. However, the average microhardness of microstructure coating and nanostructure coating prepared by the same process are 1058.5 HV0.3 and 1177.1 HV0.3, respectively [40]. With the same binder content, the average binder free path of the multimodal and nanostructure coatings decreases compared with the microstructure coatings [42]. Therefore, the hardness of the

TABLE 1: Porosity and mechanical properties of WC-CoCr coatings.

Types	Porosity (%)	K_{IC} (MPa·m$^{1/2}$)	Hardness (HV0.3)	Hardness range (HV0.3)
Microstructure coating	0.24	4.32	1058.5	919.3–1203.5
Nanostructure coating	0.51	2.70	1177.1	1042.6–1377.0
Multimodal coating	0.14	4.45	1131.2	1070.2–1285.9

WC-CoCr coatings increases with the decrease of WC particle size. Furthermore, with the decrease of WC particle size, the specific surface area of WC increases resulting in the degree of decarbonization is increased. The hardness of W_2C (~ 3000 HV) is higher than that of WC (~ 2300 HV). The content of W_2C in nanostructure coating increases, so the average microhardness of the nanostructure coating is 45.9 HV0.3 higher than that of the multimodal coating. In the measured microhardness data, the microhardness ranges of multimodal coating, microstructure coating and nanostructure coating are 215.7 HV0.3, 294.2 HV0.3 and 334.4 HV0.3, respectively. The microhardness distribution of multimodal coating is more uniform, the microhardness range of nanostructure coating is larger. This is related to the lower degree of decarbonization of the multimodal WC-CoCr coatings, resulting in a narrow range of hardness distribution of the coating (Table 1).

Figure 8 shows the indentation morphology of the coating fracture toughness measured by indentation method. It can be observed from Fig. 8(a) that cracks generated by indentation are mainly produced along the direction parallel to the interface. The fracture toughness of multimodal coating, microstructure coating and nanostructure coating prepared by the same spraying parameters is 4.45 MPa·m$^{1/2}$, 4.32 MPa·m$^{1/2}$ and 2.70 MPa·m$^{1/2}$, respectively. The multimodal coating shows the best fracture toughness. The cracks are serrated and mainly extend along the circumference of the WC particles, as shown in Fig. 8(b). When encountering large-sized WC particles, the crack growth direction is obviously deflected, and then continued to grow around the edge of WC particles. The presence of large-sized WC particles in the coating can impede the crack growth. Furthermore, the addition of nanometer WC particles in the multimodal coating increases the phase interface between WC and the bonding phase, which further hinders the crack propagation ability. However, the brittle phase W_2C content and pores in the nanostructured coating increased significantly, which reduces the fracture toughness of the coating to a certain extent.

In this study, the deposition of multimodal WC-10Co-4Cr coatings is investigated by observing the spreading morphology of individual splats on the substrate and the bonding morphology between the splats, and the mechanical properties of WC-10Co-4Cr coatings are studied. However, the more refined microscopic binding between multiple splats is not explored. The bonding between multiple splats affects the corrosion resistance as well as the wear resistance of the coating [43]. The study of the accumulation of multiple splats during the spraying process is of guiding significance for the regulation of the coating properties. In the future, the bonding between multiple splats and the effect on the internal micromorphology of the previous splat can be studied to investigate the deposition of splats with respect to the coating properties [44].

Conclusion

The multimodal WC-CoCr coating was deposited onto Q235 by HVOF. The deposition behavior of single WC-CoCr powder, microstructure, hardness and fracture toughness of the coating were investigated in this study. The main conclusions are as follows:
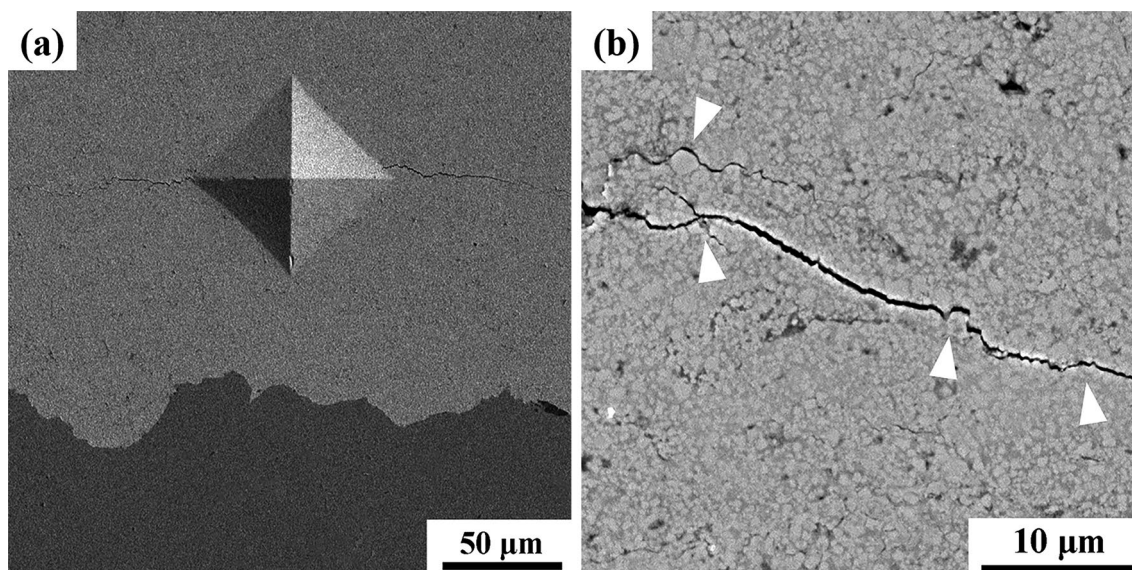

Figure 8: Microstructure of fracture toughness (a), microstructure of crack growth (b).

(1) The multimodal WC-CoCr powders are obtained by spray drying method. The multimodal WC-CoCr powders exhibit spherical morphology and closed pores inside, mainly consisting of WC, Co and Co_3W_3C phases. Most WC particles in the powders show irregular geometric shapes are embedded in the CoCr bonder phase. The splats spread on the surface of the substrate in wafer and bubble form due to the semi-molten droplets formed by the WC-CoCr powders in the HVOF process.

(2) Micron WC particles show irregular geometric shape. The WC particles with sharp corners are directly embedded into the substrate. Nano-sized WC particles show arc shape due to partial dissolution. The interface between WC grain and substrate is clear without obvious transition layer. There is a transition layer of about 100 nm between the bond phase and the substrate. Fine grain and depression deformation are observed in the substrate near the interface. The diffusion of the Fe, Cr and Co elements and occurs near the interface between splats and substrate.

(3) The multimodal WC-CoCr coating is tightly combined with the substrate without obvious cracks, pores or slag inclusions. The microstructure of the coating is dominated by WC, W_2C and Co_3W_3C phases. The porosity of the coating is 0.14%, resulting from the original morphology of the powders and the spreading morphology of the splats. The microhardness of the coating is above 1000 HV0.3. The multimodal WC particles reduce the mean free path of the bonding phase, thus increasing the hardness of the coating. The variation in hardness is reduced owing to the lower degree of decarbonization. The crack tip deflects when WC particles contact, which improves the fracture toughness of the coating.

Materials and methods

Feedstock and thermal spray process spray process

In this study, Q235 steel was selected as the substrate material. The multimodal WC-CoCr powders were manufactured by spray drying method. The multimodal WC-CoCr powders contained three sizes of WC particles of 1.5, 0.8 and 0.3 μm, with mass fractions of 15%, 66% and 5%, respectively. The size of the WC-CoCr powders is 15–35 μm. The apparent density of the WC-CoCr powders is 4.6–4.8 g/cm³.

The multimodal WC-CoCr composite coating with the thickness of about 200 μm was prepared by JP 8000 thermal spraying system. The specific spraying parameters are listed in Table 2.

TABLE 2: Spraying parameters of multimodal WC-CoCr composition coating.

Item	Kerosene (L·h⁻¹)	Oxygen (m³·min⁻¹)	Powder feed rate (g·min⁻¹)	Spraying distance mm	Surface traverse (mm·s⁻¹)
Parameter	22.71	52.38	60	380	500

Single WC-CoCr splat preparation

Multimodal WC-CoCr was deposited on Q235 steel by HVOF. Prior to spray, the substrate surface ($10 \times 10 \times 5$ mm) was polished with 1 μm diamond suspension and ultrasonically cleaned in absolute ethyl alcohol. The spray gun quickly swept the substrate surface and deposited a small number of WC-CoCr powders on the substrate surface.

Microstructure characterization

The surface morphology and microstructure of the multimodal WC-CoCr powders, coating and splats were characterized using a field emission scanning electron microscope (SEM; JEM-7800F, JEOL, Japan), with an energy dispersive X-ray spectrometer (EDS). TEM samples were prepared by Focused Ion beam (FIB; FEI, Helios G4 CX, Germany). Selected area electron diffraction (SAED) images and high-resolution transmission Electron Microscope (HRTEM) observation of the interface were performed by transmission electron microscopy (TEM; FEI, Tecnai G2 F30 S-TWIN, USA) operated at 300 kV.

The phase of powders and coating were determined using X-ray diffractometer (XRD, D8 ADVANCE, Bruker, Germany) with Cu-Kα radiation at 35 kV and 40 mA. The three-dimensional (3D) surface of the coating was observed by confocal microscopy (muSurf, NanoFocus AG, Germany). The porosity of the coatings was measured by Image J software, using no less than 15 SEM micrograph captured along the cross-section to get the average value of the porosity content.

Mechanical properties assessment

The hardness values of the polished WC-CoCr coatings were determined using a Vickers hardness indenter (MH-3, Minsks, China) under a load of 300 g and dwell time of 15 s. The average Vickers microhardness value was calculated from at least 10 indents.

The fracture toughness of the multimodal WC-CoCr coating was measured through the Vickers indenter (452-SVD, Wilson Wolpert, USA) under load of 5 kg and dwell time of 15 s. The fracture toughness was calculated by applying the Evans and Wilshaw modal in accordance with previous study [2]. At least 10 indentations were carried out for coating. The fracture toughness value was taken as the average of 10 indentations.

$$K_{IC} = 0.079 \frac{P}{a^{3/2}} \lg \frac{4.5a}{c} \qquad (1)$$

where K_{IC} is the fracture toughness (MPa·m$^{1/2}$), P is the applied load (N), a is the indentation half-diagonal length (m), and c is half of the length of the two crack tips (m). The applicable range of Eq. (1) is $0.6 \le c/a < 4.5$.

Acknowledgments

Data availability

A brief description what data or materials is available to readers and how it can be accessed, for example, a DOI to an electronic repository.

Code availability

Not applicable.

Declarations

Conflicts of interest The authors declare that they have no known competing financial interests or personal relationships that could have appeared to influence the work reported in this paper.

References

1. Z.Y. Wei, S. Hong, Z. Wei, N. Hu, G.B. Ying, Y.P. Wu, Comparison on long-term corrosion performance of WC-CoCr and Al2O3-TiO2 ceramic coatings in sulphide-containing 3.5 wt% NaCl solution. Int. J. Refract. Met. Hard Mate. **107**, 105906 (2022). https://doi.org/10.1016/j.ijrmhm.2022.105906

2. D.F. Wang, B.P. Zhang, C.C. Jia, F. Gao, Y.G. Yu, K. Chu, M.N. Zhang, X.L. Zhao, Influence of carbide grain size and crystal characteristics on the microstructure and mechanical properties of HVOF-sprayed WC-CoCr coatings. Int. J. Refract. Met. Hard Mate. **69**, 138–152 (2017). https://doi.org/10.1016/j.ijrmhm.2017.08.008

3. F. Lofaj, P. Hviščová, P. Zubko, D. Németh, M. Kabátová, Mechanical and tribological properties of the High Target Utilization Sputtering W-C coatings on different substrates. Int. J. Refract. Met. Hard Mate. **80**, 305–314 (2019). https://doi.org/10.1016/j.ijrmhm.2016.12.015

4. C.P. Jiang, J. Zhang, Y.N. Chen, Z.M. Hou, Q.Y. Zhao, Y. Li, L.X. Zhu, F.Y. Zhang, Y.Q. Zhao, On enhancing wear resistance of titanium alloys by laser cladded WC-Co composite coatings. Int. J. Refract. Met. Hard Mate. **107**, 105902 (2022). https://doi.org/10.1016/j.ijrmhm.2022.105902

5. Y. Huang, X. Ding, C.Q. Yuan, Z.K. Yu, Z.X. Ding, Slurry erosion behaviour and mechanism of HVOF sprayed micro-nano structured WC-CoCr coatings in NaCl medium. Tribol. Int. **148**, 106315 (2020). https://doi.org/10.1016/j.triboint.2020.10631

6. A.S. Marques, L.D.L.D. Costa, G.R.D. Santos, A.D.S. Rocha, Wear study of hot forging punches coated with WC-CoCr and Cr$_3$C$_2$-NiCr through high-velocity oxygen fuel (HVOF) process. Int. J. Adv. Manuf. Tech. **100**, 3–11 (2019). https://doi.org/10.1007/s00170-018-2693-3

7. Z.Q. Zhang, H.D. Wang, B.S. Xu, G.S. Zhang, Characterization of microstructure and rolling contact fatigue performance of NiCrBSi/WC-Ni composite coatings prepared by plasma spraying. Surf. Coat. Technol. **261**, 60–68 (2015). https://doi.org/10.1016/j.surfcoat.2014.11.061

8. Y. Gao, C.Q. Gao, J.Y. Gao, L. Cai, Comparison of the mechanical and wear-resistant properties of WC-13Ni4Cr and WC-10Co4Cr coatings obtained by detonation spraying. J. Therm. Spray. Technol. **28**(851), 861 (2019). https://doi.org/10.1007/s11666-019-00858-0

9. M. Nagentrau, A.L. Mohd Tobi, M. Sambu, S. Jamian, The influence of welding condition on the microstructure of WC hardfacing coating on carbon steel substrate. Int. J. Refract. Met. Hard Mate. **82**, 43–57 (2019). https://doi.org/10.1016/j.ijrmhm.2019.03.029

10. Z.X. Xie, C. Zhang, R.D. Wang, D. Li, Y.W. Zhang, G.S. Li, X.G. Lu, Microstructure and wear resistance of WC/Co-based coating on copper by plasma cladding. J. Mater. Res. Technol. **15**, 821–833 (2021). https://doi.org/10.1016/j.jmrt.2021.08.114

11. R.C. Panziera, A.C. Costa, deOliveira, Efeitos do Processo de Refusão a Laser na Microestrutura e No Comportamento de Desgaste do Revestimento de WC Aspergido com HVOF. Materia-BRazil (2019). https://doi.org/10.1590/s1517-707620190004.0808

12. I.A. Maekai, G.A. Harmain, J.H.M. Zehab-ud-Din, Resistance to slurry erosion by WC-10Co-4Cr and Cr3C2–25(Ni20Cr) coatings deposited by HVOF stainless steel F6NM. Int. J. Refract. Met. Hard Mate. **105**, 105830 (2022). https://doi.org/10.1016/j.ijrmhm.2022.105830

13. M. Wu, L. Pan, H.T. Duan, C.X. Wan, T. Yang, M.C. Gao, S.L. Yu, Study on wear resistance and corrosion resistance of HVOF

surface coating refabricate for hydraulic support column. Coatings **11**, 1457 (2021). https://doi.org/10.3390/coatings11121457

14. A.K. Gujba, M.S. Mahdipoor, M. Medraj, Water droplet impingement erosion performance of WC-based coating sprayed by HVAF and HVOF. Wear (2021). https://doi.org/10.1016/j.wear.2021.203904

15. X.L. Sun, J.K. Zhang, W.G. Pan, W.H. Wang, C.W. Tang, Research progress in surface strengthening technology of carbide-based coating. J. Alloys Compd. **905**, 164062 (2022). https://doi.org/10.1016/j.jallcom.2022.164062

16. V. Sharma, M. Kaur, S. Bhandari, Development and characterization of high-velocity flame sprayed Ni/TiO$_2$/Al$_2$O$_3$ coatings on hydro turbine steel. J. Therm. Spray Technol. **28**, 1379–1401 (2019). https://doi.org/10.1007/s11666-019-00918-5

17. T. Peat, A.M. Galloway, A.I. Toumpis, D. Harvey, Evaluation of the synergistic erosion-corrosion behaviour of HVOF thermal spray coatings. Surf. Coat. Technol. **299**, 37–48 (2016). https://doi.org/10.1016/j.surfcoat.2016.04.072

18. R. Ahmed, O. Ali, C.C. Berndt, A. Fardan, Sliding wear of conventional and suspension sprayed nanocomposite WC-Co coatings: an invited review. J. Therm. Spray Technol. **30**, 800–861 (2021). https://doi.org/10.1007/s11666-021-01185-z

19. K. Torkashvand, M. Gupta, S. Björklund, F. Marra, L. Baiamonte, S. Joshi, Influence of nozzle configuration and particle size on characteristics and sliding wear behaviour of HVAF-sprayed WC-CoCr coatings. Surf. Coat. Technol. **423**, 127585 (2021). https://doi.org/10.1016/j.surfcoat.2021.127585

20. A. Kanno, K. Takagi, M. Arai, Influence of chemical composition, grain size, and spray condition on cavitation erosion resistance of high-velocity oxygen fuel thermal-sprayed WC cermet coatings. Surf. Coat. Technol. **394**, 125881 (2020). https://doi.org/10.1016/j.surfcoat.2020.125881

21. A. Ghabchi, T. Varis, E. Turunen, T. Suhonen, X. Liu, S.P. Hannula, Behavior of HVOF WC-10Co4Cr coatings with different carbide size in fine and coarse particle abrasion. J. Therm. Spray Technol. **19**, 368–377 (2010). https://doi.org/10.1007/s11666-009-9433-z

22. L. Thakur, N. Arora, Wear behavior of WC-CoCr coatings with different carbide sizes. J. Mater. Eng. Perform. **22**, 574–583 (2013). https://doi.org/10.1007/s11665-012-0265-5

23. J.H. Yuan, C.W. Ma, S.L. Yang, Z.S. Yu, H. Li, Improving the wear resistance of HVOF sprayed WC-Co coatings by adding submicron-sized WC particles at the splats' interfaces. Surf. Coat. Technol. **285**, 17–23 (2016). https://doi.org/10.1016/j.surfcoat.2015.11.017

24. H.B. Wang, X.Z. Wang, X.Y. Song, X.M. Liu, X.W. Liu, Sliding wear behavior of nanostructured WC-Co-Cr coatings. Appl. Surf. Sci. **355**, 453–460 (2015). https://doi.org/10.1016/j.apsusc.2015.07.144

25. A. Mateen, G.C. Saha, T.I. Khan, F.A. Khalid, Tribological behaviour of HVOF sprayed near-nanostructured and microstructured WC-17wt%Co coatings. Surf. Coat. Technol. **206**, 1077–1084 (2011). https://doi.org/10.1016/j.surfcoat.2011.07.075

26. K.Y. Fan, W.H. Jiang, V. Luzin, T. Gong, W. Feng, J. Ruiz-Hervias, P.P. Yao, Influence of WC particle size on the mechanical properties and residual stress of HVOF thermally sprayed WC-10Co-4Cr coatings. Materials. **15**, 5537 (2022). https://doi.org/10.3390/ma15165537

27. I. Baumann, L. Hagen, W. Tillmann, P. Hollingsworth, D. Stangier, G. Schmidtmann, M. Tolan, M. Paulus, C. Sternemann, Process characteristics, particle behavior and coating properties during HVOF spraying of conventional, fine and nanostructured WC-12Co powders. Surf. Coat. Technol. **405**, 126716 (2021). https://doi.org/10.1016/j.surfcoat.2020.126716

28. X. Ding, Y. Huang, C. Yuan, Z. Ding, Deposition and cavitation erosion behavior of multimodal WC-10Co4Cr coatings sprayed by HVOF. Surf. Coat. Technol. **392**, 125757 (2020). https://doi.org/10.1016/j.surfcoat.2020.125757

29. P.H. Gao, C.J. Li, G.J. Yang, Y.G. Li, C.X. Li, Influence of substrate hardness transition on built-up of nanostructured WC–12Co by cold spraying. Appl. Surf. Sci. **256**, 2263–2268 (2010). https://doi.org/10.1016/j.apsusc.2009.10.050

30. S.W. Yao, C.J. Li, J.J. Tian, G.J. Yang, C.X. Li, Conditions and mechanisms for the bonding of a molten ceramic droplet to a substrate after high-speed impact. Acta Mater. **119**, 9–25 (2016). https://doi.org/10.1016/j.actamat.2016.07.057

31. W. Tillmann, L. Hagen, D. Stangier, M. Paulus, M. Tolan, R. Sakrowski, D. Biermann, D. Freiburg, Microstructural characteristics of high-feed milled HVOF sprayed WC-Co coatings. Surf. Coat. Technol. **374**, 448–459 (2019). https://doi.org/10.1016/j.surfcoat.2019.06.012

32. T. Chraska, A.H. King, Transmission electron microscopy study of rapid solidification of plasma sprayed zirconia – part II Interfaces and subsequent Splat Solidification. Thin Solid Films. **397**, 40–48 (2001). https://doi.org/10.1016/S0040-6090(01)01361-X

33. A.M. Venter, V. Luzin, D. Marais, N. Sacks, E.N. Ogunmuyiwa, P.H. Shipway, Interdependence of slurry erosion wear performance and residual stress in WC-12wt%Co and WC-10wt%VC-12wt%Co HVOF coatings. Int. J. Refract. Met. Hard Mate. **87**, 105101 (2020). https://doi.org/10.1016/j.ijrmhm.2019.105101

34. S. Kamnis, S. Gu, Numerical modelling of droplet impingement. J. Phys. D: Appl. Phys. **38**, 3664–3673 (2005). https://doi.org/10.1088/0022-3727/38/19/015

35. J.H. Kim, H.S. Yang, K.H. Baik, B.G. Seong, C.H. Lee, S.Y. Hwang, Development and properties of nanostructured thermal spray coatings. Curr. Appl. Phys. **6**, 1002–1006 (2006). https://doi.org/10.1016/j.cap.2005.07.006

36. X. Ding, X.D. Cheng, C. Li, X. Yu, Z.X. Ding, C.Q. Yuan, Microstructure and performance of multi-dimensional WC-CoCr coating sprayed by HVOF. Int. J. Adv. Manuf. Technol. **96**, 1625–1633 (2018). https://doi.org/10.1007/s00170-017-0837-5

37. X. Chen, C.D. Li, Q.Q. Gao, X.X. Duan, H. Liu, Comparison of microstructure, microhardness, fracture toughness, and abrasive wear of WC-17Co coatings formed in various spraying ways. Coatings **12**, 814 (2022). https://doi.org/10.3390/coatings12060814

38. S.I. Imbriglio, N. Brodusch, M. Aghasibeig, R. Gauvin, R.R. Chromik, Influence of substrate characteristics on single Ti splat bonding to ceramic substrates by cold spray. J. Therm. Spray Technol. **27**, 1011–1024 (2018). https://doi.org/10.1007/s11666-018-0743-x

39. L. Zhou, Z.G. Xing, H.D. Wang, P.F. He, Q.B. Mi, W.L. Guo, Y.F. Huang, L. Tang, H.F. Zhu, X.Y. Zhu, Interfacial Microstructure and Bonding Properties of Plasma-Sprayed Multilayer Ceramic Coating (Al2O3/BaTiO3/Al2O3–40 wt% TiO2). J. Therm. Spray Technol. **29**, 2012–2025 (2020). https://doi.org/10.1007/s11666-020-01097-4

40. L.Y. Chang, D.Q. Ma, W.Y. Wang, J.P. Xie, Q.B. Ji, J.C. Liu, Y.H. Song, Effect of WC grain size on characteristics of WC-10Co-4Cr composite powder and its coating properties. Trans. Mate. Heat Treat. **4**, 136–145 (2022). https://doi.org/10.13289/j.issn.1009-6264.2021-0490

41. G.C. Ji, H.T. Wang, X. Chen, X.B. Bai, Z.X. Dong, F.G. Yang, Characterization of cold-sprayed multimodal WC-12Co coating.

42. G.J. Yang, P.H. Gao, C.X. Li, C.J. Li, Simultaneous strengthening and toughening effects in WC–(nanoWC–Co). Scripta Mater. **66**, 777–780 (2012). https://doi.org/10.1016/j.scriptamat.2012.02.005

43. Y.K. Wei, Y.J. Li, Y. Zhang, X.T. Luo, C.J. Li, Corrosion resistant nickel coating with strong adhesion on AZ31B magnesium alloy prepared by an in-situ shot-peening-assisted cold spray. Corros Sci. **138**, 105–115 (2018). https://doi.org/10.1016/j.corsci.2018.04.018

44. B.D. Beake, The influence of the H/E ratio on wear resistance of coating systems-Insights from small-scale testing. Surf. Coat. Technol. **442**, 128272 (2022). https://doi.org/10.1016/j.surfcoat.2022.128272

Surf. Coat. Technol. **235**, 536–543 (2013). https://doi.org/10.1016/j.surfcoat.2013.08.021